RSC Advances

PAPER

View Article Online
View Journal | View Issue

Cite this: *RSC Adv.*, 2025, **15**, 10717

Boron carbide nanoparticles for boron neutron capture therapy†

Shiwei Xu, [a] Ying Yu, [a] Boyu Zhang, [a] Kejia Zhu,[c] Yuan Cheng[c] and Tao Zhang *[abcd]

Boron agent is widely accepted as one of the most important factors in boron neutron capture therapy (BNCT). In this study, boron carbide (B_4C) nanoparticles were subjected to chemical modification, with the folic acid moiety linked to the surface of the particles by varying the segments of the covalent linker polyethylene glycol (PEG) through γ-aminopropyltriethoxysilane (APTES) functionalization. The resultant products were three boron agents, termed as B_4C-APTES-FA, B_4C-APTES-PEG2K-FA, and B_4C-APTES-PEG5K-FA. A comparison was made between these products and the pristine B_4C nanoparticles by investigating their physicochemical properties and biological performances, including hemolysis, cytotoxicity, and cellular uptake. Subsequently, the modified B_4C-APTES-PEG2K-FA nanoparticles were subjected to *in vivo* safety assays and biodistribution investigations in mice at various dosages. Upon characterization using ICP-OES, it was found that the boron contents were the highest in the lungs, followed by the liver, spleen, kidneys, hearts, and tumors, and the lowest in the brain and muscles. The boron content in the tumor reached as high as 50 μg per g of dried tissue weight after 24 h of intravenous injection (I.V.), while the tumor-to-muscle and tumor-to-brain ratios of boron contents were found to exceed 3 following 24 hours of intravenous injection. These findings suggest that B_4C nanoparticles are promising for BNCT owing to their high boron content, satisfactory biocompatibility, and abundant chemical modification sites.

Received 31st January 2025
Accepted 14th March 2025

DOI: 10.1039/d5ra00734h

rsc.li/rsc-advances

1. Introduction

Cancer continues to be the leading cause of mortality in modern society, significantly reducing human life expectancy.[1] Boron neutron capture therapy (BNCT), a form of binary radiation therapy, was first introduced by G. Locher in 1936.[2] In 1951, W. H. Sweet and colleagues pioneered the use of BNCT for the treatment of human glioma.[3] Over the subsequent century, significant advancements have been made, with small-scale clinical studies being conducted in Japan, Finland, China and other regions;[4] the results indicate that BNCT has therapeutic benefits for malignant tumors, including melanoma, glioma, and head and neck tumors.[4] Furthermore, clinical exploratory studies on BNCT have been conducted for cancers such as genital extramammary Paget's Disease,[5] pleural tumors,[6] and hepatocellular carcinoma.[7]

The fundamental components of BNCT include a neutron source and a boron agent that is enriched with ^{10}B, which has the capacity to capture neutrons.[8,9] During the treatment, ^{10}B captures thermal neutrons and produces alpha particles (^4He) and recoil ^7Li nuclei through a nuclear fission reaction.[10] This reaction can cause damage to the DNA structure of cells at a cellular level, thereby inhibiting the growth and proliferation of tumor cells;[10] in other words, it can destroy tumor cells with great precision.[11] In the last decades, a plethora of boron agents have been developed, including borax, boric acid, and their derivatives,[12] followed by the widely used L-4-dihydroxyborylphenylalanine (BPA)[13] and sodium 1-mercaptoundecahydro-*closo*-dodecaborate ($Na_2[^{10}B_{12}H_{11}SH]$, BSH).[14] In which, the BPA has been approved for clinical treatment in Japan in 2022.[8] However, these boron agents have some limitations, such as insufficient tumor specificity, short circulating time *in vivo*, and low boron content in tumor cells, which limit their further application in BNCT.[15] Consequently, developing boron agents with enhanced targeting capabilities is a key focus of BNCT research.

Boron carbide (B_4C) is a highly chemically stable compound with high boron content widely used in industry in the form of a powder.[16] Calculations indicate that each B_4C particle, with a diameter of 200 nm, contains 460 million boron atoms. In accordance with the established criteria for BNCT, it is

[a]College of Engineering and Applied Sciences, Nanjing University, Nanjing 210023, China. E-mail: ztnj@nju.edu.cn

[b]MOE Key Laboratory of High-Performance Polymer Materials and Technology, Nanjing University, Nanjing 210023, China

[c]Wuxi Xishan NJU Institute of Applied Biotechnology, Wuxi 214104, China

[d]School of Engineering, Qinghai Institute of Technology, Xining 810016, China

† Electronic supplementary information (ESI) available. See DOI: https://doi.org/10.1039/d5ra00734h

imperative that a minimum of 10^9 ^{10}B atoms are internalized by each tumor cell to ensure the optimal therapeutic outcome.[11] Consequently, merely 2.2 particles of 200 nm B_4C uptake per tumor cell would suffice to meet these criteria. Furthermore, B_4C exhibits favorable biocompatibility[17,18] and its potential for application in BNCT has been investigated. For instance, Mortensen *et al.*[19] employed B_4C nanoparticles with a diameter of 100 nm to irradiate B16 melanoma cells with thermal neutrons, achieving complete cell death. Singh *et al.*[20] synthesized B_4C quantum dots with a diameter of 7 nm using a solvothermal method, which could rival L-BPA in clinical applications, holding promise for tumor treatment. However, large-sized pristine B_4C nanoparticles exhibit poor water dispersibility and tumor targeting. Consequently, there are challenges to be overcome if their application in biological environments is to be realized. Fortunately, the surface of B_4C particles is known to be capped with B_2O_3, which facilitates subsequent chemical reactions by chemical grafting to enhance the performance. For example, Wang *et al.*[21] demonstrated that modifying $^{10}B_4C$ nanoparticles with polyglycerol enhances their dispersibility in physiological environments, as well as their blood compatibility and biocompatibility. The *in vivo* experimental findings indicated that the modified nanoparticles exhibited low toxicity, and the ^{10}B concentration ratio in the tumor to blood is expecting to be larger than 3. Therefore, improving their tumor-targeting capabilities could make them promising boron agents for BNCT.

The folate receptor (FR) is highly expressed on the surface of many human tumor cell types,[22] while folic acid (FA) and its derivatives have been shown to specifically bind to FR, which assists their connecting nanoparticles internalized into tumor cells through receptor-mediated endocytosis.[23] Inspired by this principle, the conjugation of FA onto the surface of nanoparticles has risen as an effective strategy to achieve targeted delivery of nanoparticle.[24] Furthermore, the enhanced permeability and retention effect (EPR) has been demonstrated to improve the absorption of boron agents by tumor cells.[25,26] Following these strategies, we prepared B_4C nanoparticles *via* surface-modification with folic acid and explored their biocompatibility and biodistribution in tumor-bearing mice through comprehensive characterizations and evaluations. The results indicated that the functionalized B_4C nanoparticles in this work provide a potential BNCT agent for further investigation and application.

2. Materials and methods

2.1. Materials and instrumentations

The pristine boron carbide nanoparticles with natural boron abundance, an average diameter of 50 nm and purity of 99% were purchased from Macklin Inc (Shanghai, China). Folic acid (FA), γ-aminopropyltriethoxysilane (APTES), *N*-hydroxy succinimide (NHS), 1-ethyl-3-(3-dimethylaminopropyl) carbodiimide hydrochloride (EDC), dimethyl sulfoxide (DMSO), anhydrous ethanol, dibromomethane, and other chemicals were obtained from Aladdin Scientific Corp. (Shanghai, China). Polyethylene glycol (PEG) oligomer, with molecular weights of 2000 and 5000 daltons, both with a carboxyl group (COOH) at one end and a folic acid group (FA) at the other end, labelled as FA-PEG2K-COOH and FA-PEG5K-COOH, respectively, were supplied by Ponsure Biological Ltd (Shanghai, China). Biological reagents such as Dulbecco's Modified Eagle's Medium (DMEM), phosphate buffered saline (PBS), and fetal bovine serum (FBS) were purchased from Thermo Fisher Scientific (Shanghai, China). Cell Counting Kit-8 (CCK-8), fluorescein isothiocyanate (FITC) cell membrane red fluorescent probe DiI, and Hoechst 33 342 were purchased from Beyotime Biotechnology (Shanghai, China). The cell lines, including HepG2, A549, and L929 were obtained from Cellcook Ltd (Guangzhou, China). NCG mice (NOD/ShiltJGpt-Prkdc^{em26Cd52}Il2rg^{em26Cd22}/Gpt, SPF grade) and nude mice (BALB/c-nu, SPF grade) were acquired from GemPharmatech Co., Ltd (Nanjing, China). Porcine blood was purchased from SenBeiJia Biological Technology Co., Ltd (Nanjing, China).

In terms of instrumentation, X-ray photoelectron spectroscopy (XPS) data were collected using a Scientific K-Alpha photoelectron spectrometer (Thermo Fisher Scientific, USA). The concentration of elemental boron was determined using an Avio 220 Max inductively coupled plasma optical emission spectrometer (ICP-OES) (PerkinElmer, USA) and the samples were prepared using a M3 microwave digestion system (PreeKem, China) for the digestion of boron carbide and other substances. Dynamic light scattering (DLS) data were collected using a Litesizer 500 scatterometer (Anton Paar, Austria). Transmission electron microscopy (TEM) images were obtained using a JEM-1400 electronic microscope (JEOL, Japan), and the samples were prepared on a copper mesh with 200-mesh carbon support film at a voltage of 120 kV. Thermogravimetric analysis (TGA) was performed using a STA409PC analyzer (Netzsch, Germany) in a N_2 atmosphere at a heating rate of 20 °C min^{-1} from room temperature to 600 °C. Fourier transform infrared (FTIR) spectra were recorded on a FTIR-650 infrared spectrometer (Gangdong, China). Ultraviolet-visible (UV-vis) absorption spectra were recorded on a UV3600 spectrometer (Shimadzu, Japan). Fluorescence spectra (FS) were obtained using an LS-55 spectrometer (PerkinElmer, USA). Fluorescence images were captured on an FV3000 confocal laser scanning microscope (CLSM) (Olympus, Japan).

2.2. Chemical modification and characterization of B_4C nanoparticles

The chemical modifications on B_4C nanoparticles were conducted as shown in Scheme 1. Typically, the pristine B_4C powder with a nominal average size of 50 nm was dispersed in water and ultrasonicated for 10 minutes, then centrifuged at 2000 rpm for 10 minutes to remove the large particles. The supernatant was collected by evaporation to obtain the pure B_4C nanoparticles (NPs). At room temperature, approximately 1 g of B_4C NPs was added to a mixed solvent consisting of 150 mL of dibromoethane and 50 mL of anhydrous ethanol. To this mixture, 500 μL of acetic acid and 0.5 g of APTES were added and stirred for 12 h at room temperature.[26,27] After evaporation and vacuum drying, B_4C-APTES was obtained.

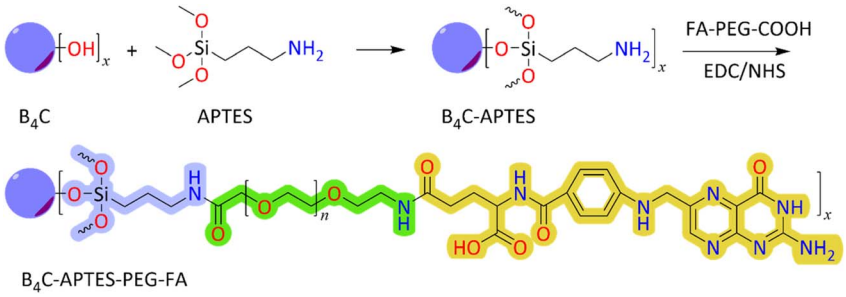

Scheme 1 Modification route for B_4C nanoparticles.

Under a N_2 atmosphere, 0.44 g of folic acid, 2.44 g of FA-PEG2K-COOH, or 5.44 g of FA-PEG5K-COOH were dissolved separately in 20 mL of dry DMSO, to which, 383 mg of EDC, 115 mg of NHS and 825 μL of pyridine were added. The mixture was stirred overnight at room temperature. Then, 0.25 g of B_4C-APTES was added to the mixture and stirred for 2 days. The mixture was then centrifuged at 10 000 rpm for 10 minutes. The yellowish supernatant was removed and the NPs were washed with 10 mL DMSO and centrifuged at 10 000 rpm for a further 10 minutes. The process was repeated until the supernatant was almost colorless. The NPs were then washed with ethanol and centrifuged at 10 000 rpm for 10 minutes, followed by vacuum drying at room temperature.[26,27] Finally, three boron agent products were obtained: B_4C-APTES-FA, B_4C-APTES-PEG2K-FA, and B_4C-APTES-PEG5K-FA.

2.3. *In vitro* biocompatibility investigations

The hemolysis assay of different B_4C NPs was evaluated using porcine blood. In detail, 4 mL of heparin-anticoagulated porcine blood was mixed with an equal volume of saline in a 15 mL centrifuge tube, centrifuged at 4000 rpm for 10 minutes, and the supernatant was then removed. To separate the erythrocytes, a volume of normal saline equivalent to 2–3 times the volume of erythrocytes was added, gently mixed, and then centrifuged at 4000 rpm for 5 minutes at 4 °C, and the supernatant was discarded. After at least three repeats, the remaining supernatant was removed and an appropriate volume of normal saline was added to prepare a 2% erythrocyte suspension.

Pure B_4C NPs and modified B_4C-APTES-FA, B_4C-APTES-PEG2K-FA, and B_4C-APTES-PEG5K-FA NPs were dispersed in saline respectively at concentrations of 6.25, 12.5, 25, 50, 100, and 200 μg mL^{-1} (calculated by the mass of elemental boron). For each dispersion, 0.75 mL was pipetted into an EP tube, followed by the addition of 0.75 mL of a 2% erythrocyte suspension. At the same time, 0.75 mL of normal saline was used as a negative control group and 0.75 mL of pure water as a positive control. All samples were incubated at 37 °C for 1 hour and then centrifuged at 12 000 rpm for 10 minutes. The supernatant was collected and dispensed into a 96-well plate, and the absorbance (OD) was measured at a wavelength of 540 nm. The hemolysis rate was calculated using the following formula:

$$\text{Hemolysis rate} = \frac{OD_{Ex} - OD_{Nc}}{OD_{Pc} - OD_{Nc}} \times 100\%$$

where Ex, Nc, and Pc represent the experimental, negative control and positive control group, respectively.

The cytotoxicity of NPs was evaluated against L929, A549, and HepG2 cell lines, respectively. Using 96-well plates, cells were cultured at a density of 5000 cells per well in DMEM (supplemented with 10% FBS and 1% penicillin-streptomycin) at 37 °C and a 5% CO_2 atmosphere for 24 hours. The culture medium was then replaced with 100 μL DMEM dispersions containing B_4C series NPs at the doses of 3.125, 6.25, 12.5, 25, 50, and 100 μg mL^{-1} (calculated from the mass of elemental boron) and incubated for a further 24 and 48 hours. Five wells were used per dose. Cell viability was then determined using the CCK-8 assay. After the addition of CCK-8 reagent, the cells were incubated for another 1 hour and the absorbance was measured at 450 nm, with the cell viability calculated using the following formula:

$$\text{Cell viability} = \frac{OD_{Ex} - OD_{Blk}}{OD_{Ctl} - OD_{Blk}} \times 100\%$$

where Ex, Ctl, and Blk represent the experimental, control and blank group, respectively.

The cellular uptake determination was conducted using FITC-labeled B_4C-APTES-PEG2K-FA nanoparticles. The isothiocyanate group (–N=C=S) of FITC reacted with the amino group ($–NH_2$) of folic acid to form a stable thiourea linkage (–NH–CS–NH–). Specifically, 5 mg of FITC was dissolved in 0.5 mL of ethanol and added into a 5 mL dispersion of B_4C-APTES-PEG2K-FA in water, with a concentration of 1 mg mL^{-1}. Following a one-hour incubation period, the dispersion was subjected to centrifugation at 10 000 rpm for 5 minutes, after which the supernatant was discarded. The NPs were then washed and re-centrifuged thrice in pure water, after which they were lyophilized and designated as B_4C-APTES-PEG2K-FA-FITC.

In 20 mm confocal Petri dishes, 10^3 cells per well of HepG2 and A549 were respectively inoculated and incubated at 37 °C and a 5% CO_2 atmosphere for 24 hours. Thereafter, the medium was substituted with 1 mL of medium containing 10 μg of B_4C-APTES-PEG2K-FA-FITC and the dish was left to incubate for a further 24 hours. Subsequently, DiI and Hoechst 33 342 were utilized for the staining of cell membranes and cell nuclei, respectively, in accordance with the protocols provided by the manufacturers, and the staining process was conducted in the

darkness for a duration of 10 minutes for each dye. Followed by fixation with 1 mL of paraformaldehyde for 15 minutes and washing with PBS, the cells were observed using an FV3000 confocal laser scanning microscope.

2.4. *In vivo* safety and biodistribution investigations

The animal experiments of this study have been approved by the Science and Technology Ethics Committee of Nanjing University (Approval No. IACUC-2312013), ensuring adherence to ethical standards. First, the acute toxicity of nanoparticles was explored in nude mice. Nine nude mice were randomly divided into three groups with three mice per group. The mice in the experimental groups were injected with 200 μL of normal saline containing B_4C-APTES-PEG2K-FA at a dosage of 10 mg kg^{-1} or 30 mg kg^{-1} through the tail vein, respectively, calculated from the mass of elemental boron. The control group received normal saline injections through the tail vein. At 24 hours and 168 hours post-injection, respectively, the mice were anesthetized, and the blood was collected *via* the abdominal aorta for further analysis. At 24 hours post-injection, the nude mice were euthanized and dissected. The vital tissues, including the hearts, livers, spleens, lungs, and kidneys, were fixed in 4% paraformaldehyde, and subsequently embedded in paraffin. Sections were prepared and stained with hematoxylin and eosin (H&E), and observed using a digital pathological section scanner.

Subsequently, the biodistribution of nanoparticles was investigated in tumor-bearing NCG mice. The experimental design involved the division of 20 NCG mice at 4 weeks of age and weighing 18 grams with implanted HepG2 cells in the axillary regions, with a solid tumor volume of approximately 200 mm^3. The mice were divided into two groups: 4 mice in the control group and 16 in the experimental group. The experimental groups received 200 μL of saline containing B_4C-APTES-PEG2K-FA at a dosage of 30 mg kg^{-1}, calculated from the mass of elemental boron *via* tail intravenous injection (I.V.), while the control group received normal saline. At 6-, 24-, 48-, and 72-hours post-injection, respectively, four mice from the experimental group and one mouse from the control group were euthanized and sacrificed to collect blood, heart, liver, spleen, lungs, kidneys, tumors, whole brain, and muscle, respectively. A random selection of organs from one mouse at each sampling time were subjected to freezing, sectioning, and hematoxylin and eosin (H&E) staining for further observation. Meanwhile, the remaining organs from the other three mice were lyophilized, weighed, and subjected to a microwave-assisted digestion in a mixture of H_2SO_4, HNO_3, and HF solution. The boron content was subsequently determined by inductively coupled plasma-optical emission spectroscopy (ICP-OES).

3. Results and discussion

3.1. Modification and characterization of boron carbide nanoparticles

First, the morphology of the nanoparticles was observed by TEM, as shown in Fig. 1A. The size distribution of the series of B_4C NPs was relatively wide, ranging from 50 nm to 100 nm. Notably, the dispersal state of B_4C-APTES-PEG2K-FA and B_4C-APTES-PEG5K-FA nanoparticles was enhanced compared with pristine B_4C NPs and B_4C-APTES-FA that could be attributed to the hydrophilic structure of PEG on the nanoparticle surface, which facilitated their dispersal in solutions and reduced agglomeration when deposited on copper meshes. The yields of B_4C-APTES, B_4C-APTES-FA, B_4C-APTES-PEG2K-FA, and B_4C-APTES-PEG5K-FA NPs were found to be 95.3%, 88.1%, 88.9%, and 84.2%, respectively, indicating efficient conjugation during the process.

To illustrate this phenomenon visually, the dispersion of the series of B_4C NPs (10 μg mL^{-1}) in 0.01 M PBS (pH = 7.4) was compared, as demonstrated in Fig. 1B. Following ultrasonic treatment, numerous particles were dispersed in a consistent and even manner with the PBS. However, the stability of B_4C-APTES was found to be inadequate, with agglomeration and sedimentation being observed within approximately 96 hours. Conversely, other concentrated nanoparticles exhibited superior dispersion stability, maintaining their dispersity for approximately 10 days. Due to the instability of folic acid and APTES under high temperatures and overly acidic or alkaline conditions, nanoparticles are also unstable in these extreme environments (see Fig. S1 in the ESI† for details).

To further explore the stability of nanoparticles, DLS was utilized to continuously monitor the hydrodynamic diameter and ζ potential of NPs was also recorded over a period of two months, as illustrated in Fig. 1C. For NPs dispersed by ultrasound, the B_4C NPs demonstrated the smallest average hydrodynamic diameter of 216 nm, followed by B_4C-APTES with 233 nm. The average hydrodynamic diameters of B_4C-APTES-FA, B_4C-APTES-PEG2K-FA, and B_4C-APTES-PEG5K-FA increased slightly, with values of 240 nm, 250 nm, and 260 nm, respectively. These increases in size could be attributed to the connection of FA and its PEGylated derivatives. It is noteworthy that due to the presence of a solvent shell around the particles, the hydrodynamic diameter is usually larger than the actual diameter. This phenomenon explains why the particle sizes measured by DLS were larger than those observed by TEM. Over the course of 60 days, the particle sizes of B_4C-APTES-FA, B_4C-APTES-PEG2K-FA and B_4C-APTES-PEG5K-FA increased slightly, although they remained relatively stable overall. In contrast, the particle size of B_4C-APTES changed significantly and was not as stable as the PEGylated ones in PBS solution, aligning with the previous observations.

The surface charge of nanoparticles was analyzed by ζ potential (Fig. 1C). The presence of a significant number of boric acid groups on the surface of B_4C resulted in its negative charge. However, following the coupling of APTES, a shift in surface charge towards a positive state was observed. This transformation was attributed to a reaction between the boronic acid group and the methoxy group of APTES, whereby the NH_2 of APTES combined with the H^+ ion in the solution to form NH_3^+. This process resulted in the transformation of the surface charge from negative to positive. Following functionalization with folic acid and its pegylated derivatives, the three types of nanoparticles returned to negative charge. This reversal was due

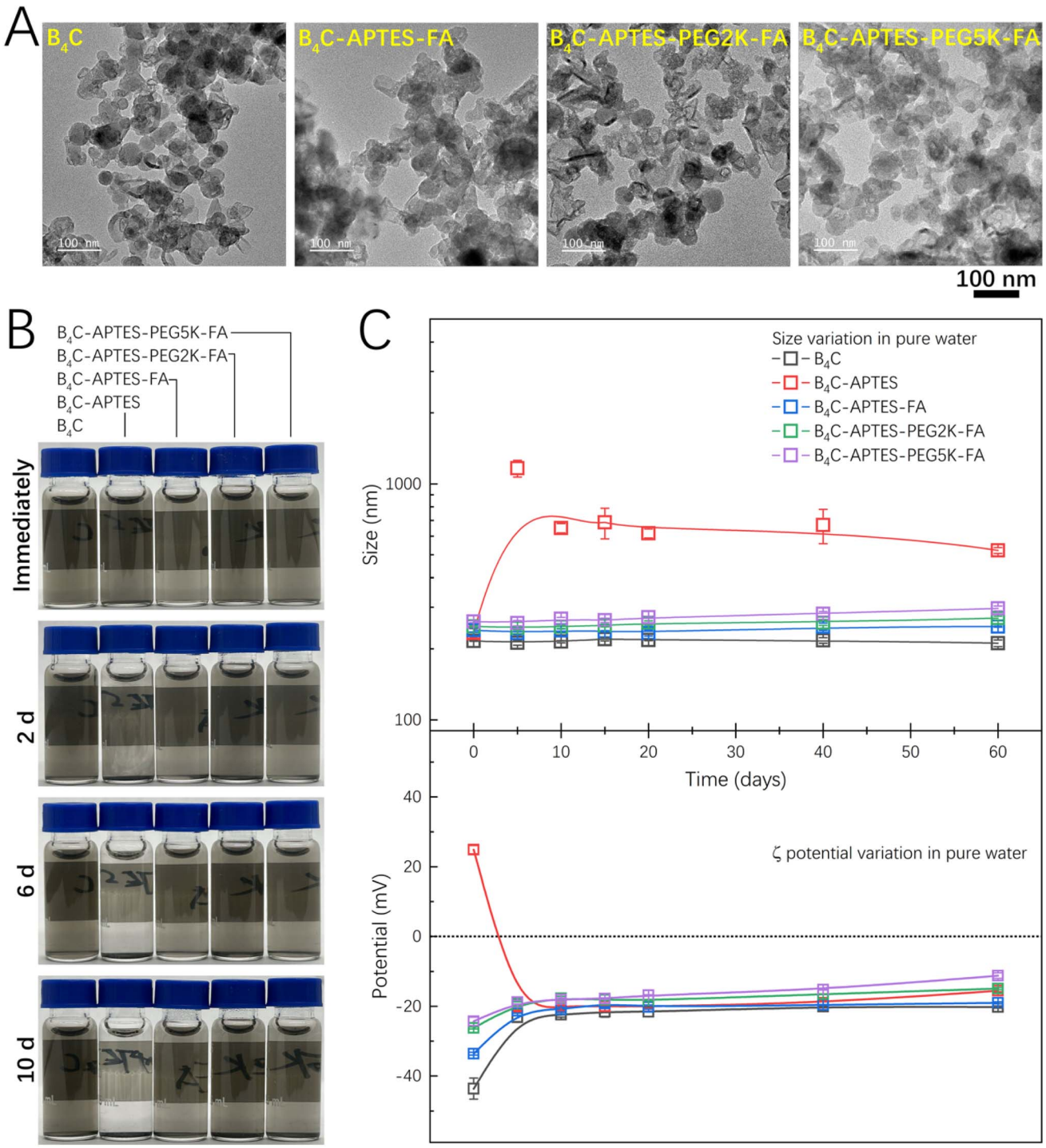

Fig. 1 Micromorphology and aqueous dispersity of B_4C nanoparticle and its modified derivatives. (A) Transmission electron microscopy (TEM) images. (B) Dispersion stability of the nanoparticles (10 μg mL^{-1} in PBS). (C) The 60 day measurement of hydrodynamic diameter and ζ potential.

to the reaction between the amino groups on their surface and the carboxyl groups of folic acid. Concurrently, the carboxyl group on folic acid underwent ionization, yielding a negative charge on the nanoparticle surface. The B_4C-APTES sample switched to negative zeta potential after a few days, because the ethoxy groups of B_4C-APTES undergo hydrolysis, forming silanol groups (–SiOH); these silanol groups can further dissociate in solution, releasing H^+ ions and resulting in a negatively charged surface (–SiO–).

In summary, the three modified NPs exhibited superior stability in PBS when compared with B_4C-APTES. This enhanced stability is a prerequisite for potential biomedical applications, where it is essential for NPs to remain dispersed over an extended period.

To ascertain the structure of a series of boron carbide modifications and subsequently validate the properties of the resultant nanoparticles, comprehensive physical and chemical characterizations were conducted.

The elemental composition and molecular structure of the nanoparticles were investigated using XPS. As demonstrated in Fig. 2A, the B_4C spectrum exhibited C 1s (284–290 eV), O 1s (529–535 eV) and B 1s (187–193 eV) peaks in the B_4C spectrum. These findings confirmed that the surface of B_4C was covered by B_2O_3, which promoted the formation of hydroxyl and laid the foundation for the subsequent reaction. Furthermore, the presence of a Si 2p peak at approximately 100 eV was observed in the spectrum of B_4C series modifiers, indicating the successful introduction of the Si element. This finding also indirectly confirmed the successful connection of APTES. As demonstrated in Fig. 2B, the intensive scanning of the C 1s spectra enabled the discernment of distinct carbon bonds within the B_4C spectra. Specifically, the binding energy of 284.2 eV was ascribed to the B–C bond, 285.1 eV to the C–C bond, and 286.8 eV to the C–O bond. In the spectrum of the B_4C series modified products, four peaks were identified, corresponding to four different states of the C element. The binding energy at approximately 281.5 eV was related to B–C bonds, 283–285 eV was related to C–C bonds, 285–287 eV was related to C–O bonds, and 289 eV was related to O–C=O bonds.[28–30] Following the modification process, a notable increase in the variety and quantity of carbon bonds were observed.

The functional groups present on the surface of the NPs were analyzed by FTIR, the results of which are shown in Fig. 2C. The surface of B_4C was found to contain a significant number of oxygen-containing functional groups. The band at 3425 cm^{-1} corresponds to the –OH. Following the surface modification of B_4C by APTES, a stretching vibration absorption peak of Si–O was observed at 1100 cm^{-1}. Following further reaction with folic acid, the stretching vibration absorption peak of –C=O belonging to folic acid appeared at 1625 cm^{-1}. The bands at 2840 cm^{-1} and 2920 cm^{-1} confirmed the presence of $-CH_2$ groups. This outcome demonstrated the successful conjugation of folic acid.

As demonstrated in Fig. 2D, the TGA results provide information on the thermal stability and composition of the various samples. The weight loss of B_4C at 600 °C was 4.3%, which was primarily due to the removal of water and organic components on the surface. For B_4C-APTES, the weight loss at 600 °C increased to 9.3%, with the additional loss being due to the decomposition of the $-CH_2CH_2CH_2NH_2$ group introduced by APTES. The loss of the organic portion was approximately 5%; that is to say, there was about 0.86 mmol of the $-NH_2$ group per gram of NPs. Following the functionalization of NPs with folic acid and its derivatives, the weight loss of B_4C-APTES-FA, B_4C-APTES-PEG2K-FA, and B_4C-APTES-PEG5K-FA at 600 °C increased to 13.8%, 15.2%, and 17.6%, respectively. To ensure that the observed weight loss was not attributable to surface-adsorbed folic acid, the NPs were thoroughly washed. Consequently, the observed weight loss (excluding water and unreacted $-CH_2CH_2CH_2NH_2$ groups) was primarily attributed to the loss of attached folic acid and its PEGylated derivatives. This finding indicated that the percentages of folic acid and its PEGylated derivatives decorated on the three NPs were 4.5%, 5.9%, and 8.3%, respectively.

As shown in Fig. 2E and F, the optical properties of the nanoparticles were characterized by UV-Vis and fluorescence spectra. FA exhibited an absorption band at 281 nm. Following the attachment of the FA moiety to the surface of the particles with or without polyethylene glycol, a weak absorption band was observed at 281 nm, indicative of the presence of FA. To further explore the fluorescence properties, excitation at 283 nm was employed. FA exhibited a strong fluorescence emission peak at 441 nm. It was noteworthy that B_4C itself exhibited no discernible absorption or emission bands. However, B_4C-APTES-FA, B_4C-APTES-PEG2K-FA, and B_4C-APTES-PEG5K-FA all exhibited fluorescence emission peaks at 441 nm, indicating that folic acid or its pegylated derivatives had been successfully coupled with the NPs.

Consequently, the above series of characterizations demonstrated the successful coupling of FA or its PEGylated derivatives to nanoparticles, thereby establishing the foundation for further exploration of the potential application of these functional nanoparticles.

3.2. *In vitro* biocompatibility of modified B_4C nanoparticles

The hemolysis assay is one of the key assessments to determine the biological safety and blood compatibility of nanoparticles.[31] If nanoparticles cause serious damage to red blood cells after entering the body, it can lead to serious health problems such as high blood pressure and anemia.[32] As demonstrated in Fig. 3A, the three as-prepared nanoparticles did not exhibit significant hemolysis at concentrations ranging from 6.25 to 200 μg mL^{-1}. This finding suggests that these functionalized nanoparticles possess good blood compatibility. The hemolysis rate of B_4C gradually increased, reaching a maximum value of 4.74% at 200 μg mL^{-1}, but this was still within the safe range (no more than 5%).[33,34] The hemolysis rate of functionalized nanoparticles was lower than that of B_4C, which might be attributed to the conjugated PEG and FA.

Cytotoxicity experiments were conducted to evaluate the effect of nanoparticles on cell viability. When cells were exposed to nanoparticles, the nanoparticles affected cell metabolism and protein synthesis, thereby influencing cell viability. The following cell lines were utilized in this experiment: L929, a mouse fibroblast cell line; A549 cells,[35] a human non-small cell lung cancer cell line with low folate receptor (FR) expression; and HepG2 cells,[36] a human liver carcinoma cell line with high FR expression. The nanoparticles were co-cultured with the cells for 24 hours and 48 hours, and the cell viability was detected using the CCK-8 assay. As demonstrated in Fig. 3B, the results indicated that for A549 and L929 cells, the level of cytotoxicity was relatively low when the concentration of boron was low. It is noteworthy that even at a concentration of 25 μg mL^{-1}, cell viability remained above 60%. Conversely, for HepG2 cells, FA-modified NPs demonstrated a heightened level of cytotoxicity in comparison to B_4C NPs at a maximum concentration of 100 μg mL^{-1} of boron. This observation can be attributed to the high expression of FRs on HepG2 cells, which

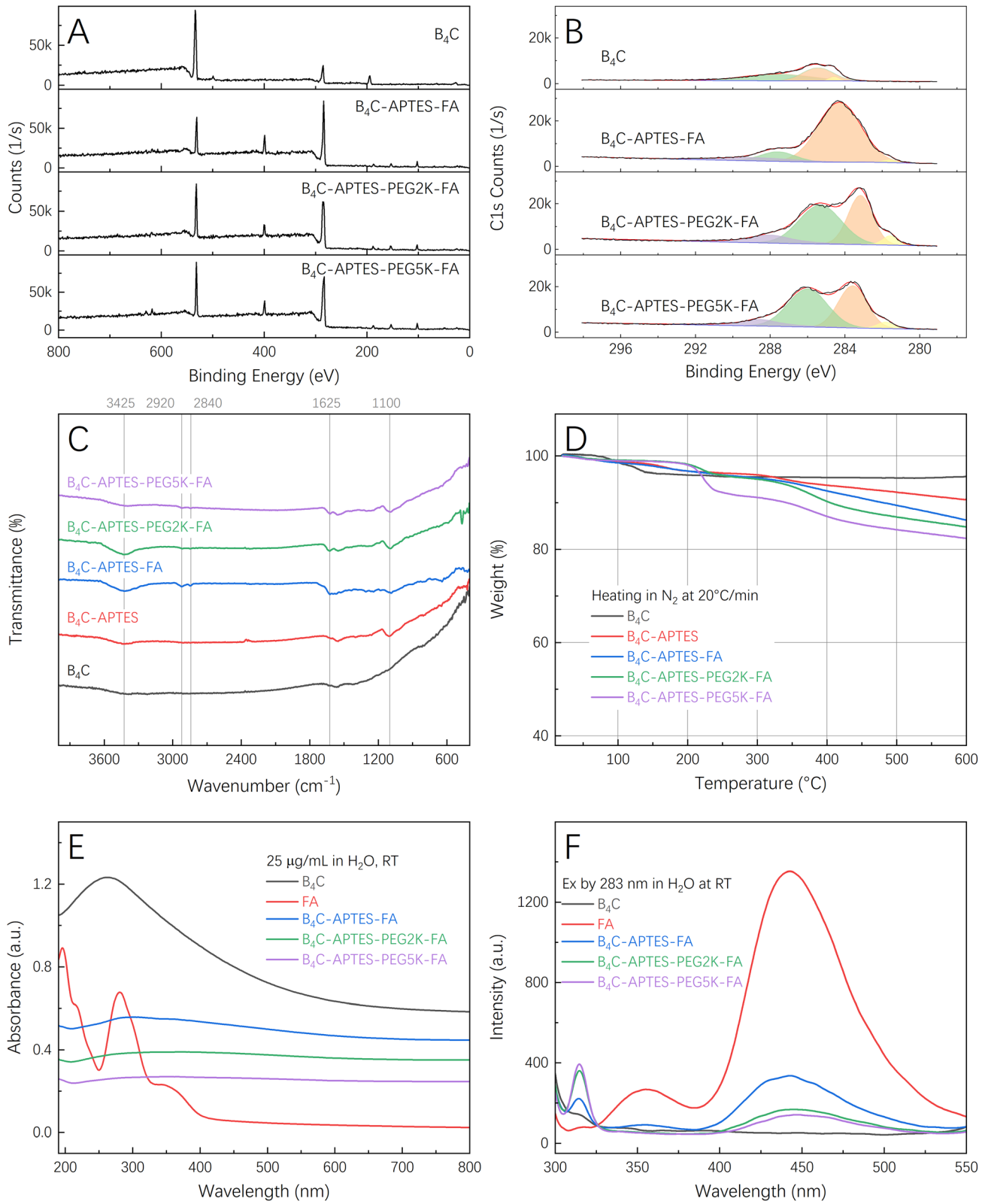

Fig. 2 Chemical characterizations of B_4C nanoparticle and its derivatives. (A) XPS survey scans. (B) XPS C 1s intensive scans. (C) FTIR spectra. (D) TGA curves of nanoparticles. (E). UV-Vis spectra of nanoparticles. (F) FS spectra of nanoparticles.

facilitated the binding of more modified nanoparticles, thereby increasing the likelihood of the nanoparticles entering the cells and interfering with their growth. Real-time cell analysis (RTCA) assays will be used for cytotoxicity experiments in the future because they can be employed for the viability evaluation of nanoparticle-exposed cells as a function of time.[37,38]

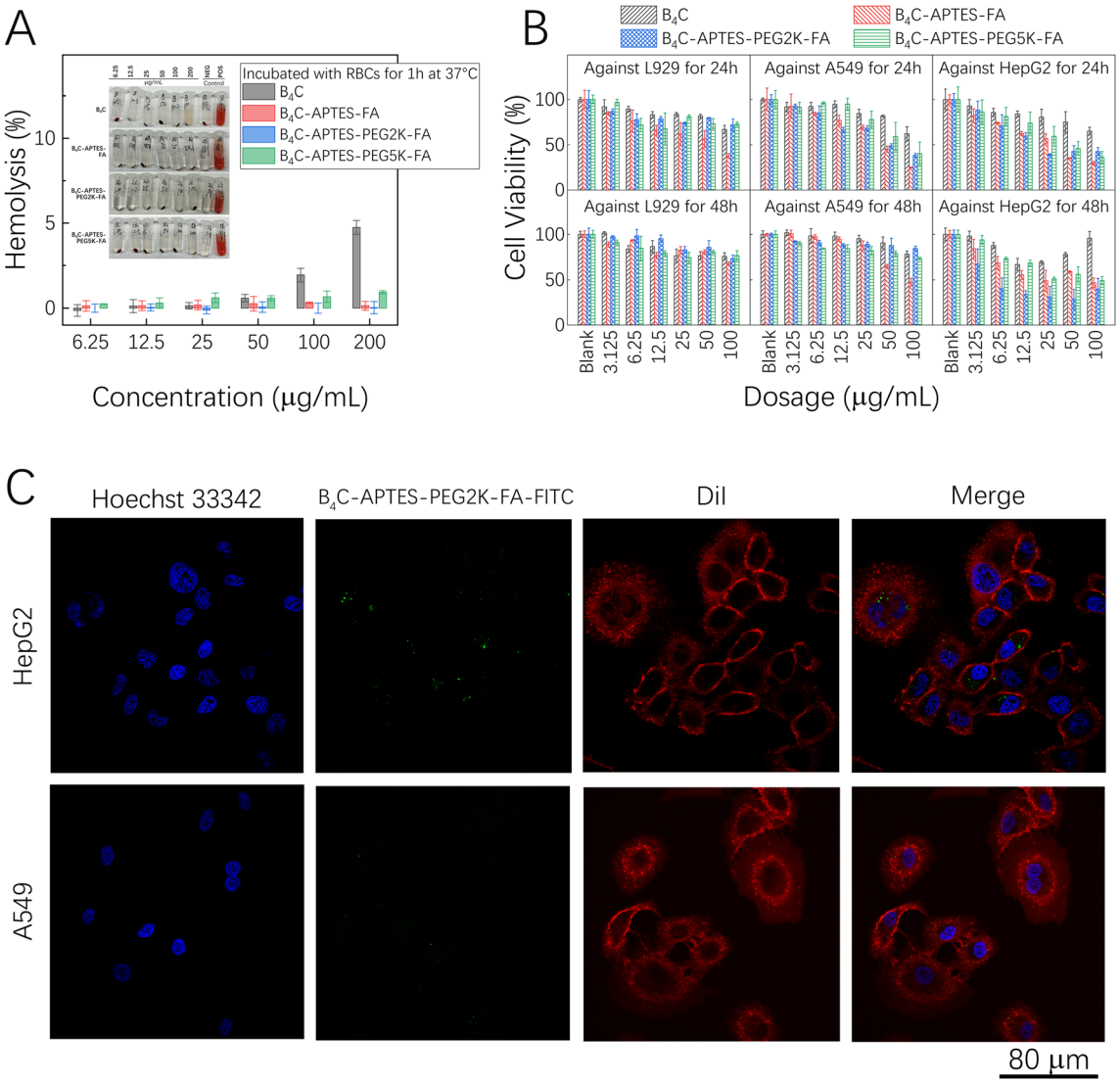

Fig. 3 *In vitro* biocompatibility of modified B_4C nanoparticles. (A) Hemolysis rate of nanoparticles with the inset depicting representative images of hemolysis images at varying concentrations. (B) Cytotoxicity of nanoparticles against the L929, A549, and HepG2 cell lines following 24- and 48-hours of exposure. (C) Cellular uptake of nanoparticles (incubated for 24 hours); images were captured using a confocal laser scanning microscope.

FR is a glycoprotein to which FA can bind specifically. FR is overexpressed on the surface of HepG2 cell membrane[36,39,40] and under expressed on the surface of A549 cell membrane. As demonstrated in Fig. 3C, the cell membranes were stained with DiI, which was excited by a laser with a wavelength of 405 nm, rendering them red. The cell nuclei were stained with Hoechst 33 342, which was excited by a laser emitting a wavelength of 346 nm, rendering them blue. The B_4C-APTES-PEG2K-FA-FITC nanoparticles were excited by a laser at 488 nm, resulting in an observable green in the images. It was evident that HepG2 cells exhibited a higher accumulation of green-emitting particles, indicative of enhanced internalization of B_4C-APTES-PEG2K-FA-FITC. In contrast, A549 cells displayed a reduced uptake of the NPs and a concomitant decrease in green emitting particles. HepG2 cells exhibited higher fluorescence intensity in comparison to A549 cells, with the majority of the fluorescence being observed in the cytoplasm. This discrepancy in uptake can be attributed to the differential expression levels of FR on the cell surfaces. According to previous reports, the surface of a single A549 cell expresses approximately $(10.44 \pm 0.53) \times 10^{-19}$ mol of FR, and the surface of a single HepG2 cell expresses $(337.14 \pm 10.11) \times 10^{-19}$ mol of FR,[41] which is approximately 32 times that of a single A549 cell. Given that NPs were functionalized with FA, they exhibited a higher affinity for cells expressing FR. Consequently, B_4C-APTES-PEG2K-FA-FITC exhibited a greater propensity to bind to the abundant FR on the HepG2 cell surface compared to the A549 cells, thereby facilitating the accumulation of the nanoparticles on or near the HepG2 cell surface, and increasing the likelihood of their endocytosis into the cells. To further confirm that NPs entered cells *via* endocytosis, the NPs and cells were co-cultured at 4 °C for 24 hours. No green fluorescence emission was observed in the cytoplasmic region, which

provided further evidence supporting the endocytosis-mediated uptake of NPs (see Fig. S2 in the ESI† for details).

3.3. *In vivo* safety studies and biodistribution in mice

The *in vivo* biosafety of nanoparticles was investigated by conducting blood routine tests on healthy nude mice 24 hours after I.V. injection. Subsequently, blood biochemistry tests were performed at 24- and 168-hours post-injection (for specific results, refer to ESI Tables S1 and S2†). Following the tail injection, the mice were euthanized 24 hours after the administration and dissected to procure hearts, livers, spleens, lungs, and kidneys. Tissue samples were then prepared and stained with H&E for subsequent observation, as shown in Fig. 4A.

Based on the premise of ensuring biological safety, the biodistribution of nanoparticles in tumor-bearing NCG mice was further explored. At 6-, 24-, 48-, and 72-hours post-injection, the hearts, liver, spleen, lungs, kidneys, tumors, whole brains, and muscle were harvested, as shown in Fig. 4B. Following digestion, the boron content was quantitatively analyzed using ICP-OES. Additionally, tumor tissues collected at four different time points were processed into frozen sections and stained with H&E for observation, as shown in Fig. 4C and D.

As demonstrated in Table S1,† the results of the blood routine analysis of nude mice following tail intravenous injection over a 24 hours period indicate that their primary biochemical indicators fall within the normal physiological range. Moreover, no statistically significant disparities were observed between the experimental group and the control group, which partially supports the safety of the nanoparticles.

Table S2† presents the results of blood biochemical test conducted on nude mice at 24 hours and 168 hours following injection. The results demonstrated that the concentrations of alanine aminotransferase (ALT), aspartate aminotransferase (AST), albumin and urea nitrogen (BUN) increased marginally 24 hours after tail vein injection, yet no statistically significant differences were observed when compared with the control group. However, after 168 hours of metabolism, the concentrations of AST, albumin and BUN generally returned to the same level as the control group (see Table S2†). Additionally, the indicators of renal function, namely creatinine and BUN metabolism, did not undergo a rapid or significant increase, suggesting that the NPs did not elicit acute kidney failure in the mice.[42] However, 24 hours post-injection, a more pronounced increase in the two renal function indicators, creatinine, and uric acid, was observed when compared to the control group, although statistical evaluation revealed no significant difference. Nevertheless, after 168 hours, these two indicators demonstrated a significant divergence from their 24 hours values. A decrease in creatinine indicated an increase in glomerular filtration rate or enhanced tubular secretion function in mice, while a decrease in uric acid indicated an increase in purine metabolism in mice. These observations indicated that there were no significant abnormalities in renal metabolism in mice. However, given the various factors that affected creatinine and uric acid levels, further medical examinations were necessary.

In summary, compared with the control group, there were no significant abnormalities in the liver and kidney function of the experimental group mice. This finding attests to the fact that the NPs did not elicit acute damage in mice. Additionally, the blood routine and biochemical indicators of the mice were indistinguishable from those of the healthy control group of nude mice. Consequently, the B_4C-APTES-PEG2K-FA NPs exhibited substantial impact on the hematopoietic function and metabolism of mice, thereby demonstrating favorable biological safety.

Subsequently, the distribution of boron in the heart, liver, spleen, lung, and kidney of healthy nude mice was investigated. As illustrated in Fig. 4A, H&E staining revealed the presence of nanoparticles in the lungs, manifesting as black micron-sized aggregates. This phenomenon can be attributed to the intravenous injection of NPs, which subsequently circulated through the bloodstream. The pulmonary capillaries were the primary site of nanoparticle interception, resulting in a darker appearance of the lungs.

Additionally, smaller black particles were discernible in the liver and spleen, although they were virtually undetectable in the heart. Histological analysis of H&E-stained sections revealed no discernible lesions, suggesting that the NPs did not cause significant damage to the primary organs and tissues. According to reports, particles exceeding 2000 nm in size tend to accumulate within the capillaries of the lungs, while NPs larger than 150 nm are readily captured by the liver and spleen.[43] Furthermore, particles sized between 100–200 nm have been observed to exploit the enhanced permeability and retention (EPR) effect, thereby evading filtration by the liver and spleen.[44] Meanwhile, particles measuring less than 5 nm are filtered out by the kidneys.[45] It is also noteworthy that neutral and negatively charged NPs possess extended circulation lifetimes.

The experiments conducted in this study have already demonstrated the biological safety of the NPs, and the biodistribution of these NPs has been broadly understood through H&E stained sections. However, to obtain a more comprehensive understanding, further quantitative analysis was necessary to investigate the biodistribution and enrichment of boron in tumor-bearing NCG mice. To this end, mice were subjected to a series of dissections at 6-, 24-, 48-, and 72-hour intervals post-injection to assess organ pathology. As demonstrated in Fig. 4B, the organs of the control group mice exhibited a healthy, rose-colored appearance at the indicated time points. In contrast, the liver, spleen, and lung of mice in the experimental group presented with a black appearance, suggesting the presence of a substantial number of particles within these tissues. This phenomenon can be attributed to the presence of a substantial number of black particles that were captured by phagocytes. A salient observation was the darker coloration of the tumors in the experimental group compared to the control group. This discrepancy can be attributed to the enrichment of NPs within the tumors of the experimental group, a phenomenon facilitated by the EPR effect, which resulted in a darker appearance.

Frozen sections of NCG mice were monitored over a period of 72 hours. As illustrated in Fig. 4C and D, the preliminary observation conducted at 6 hours post-injection revealed the

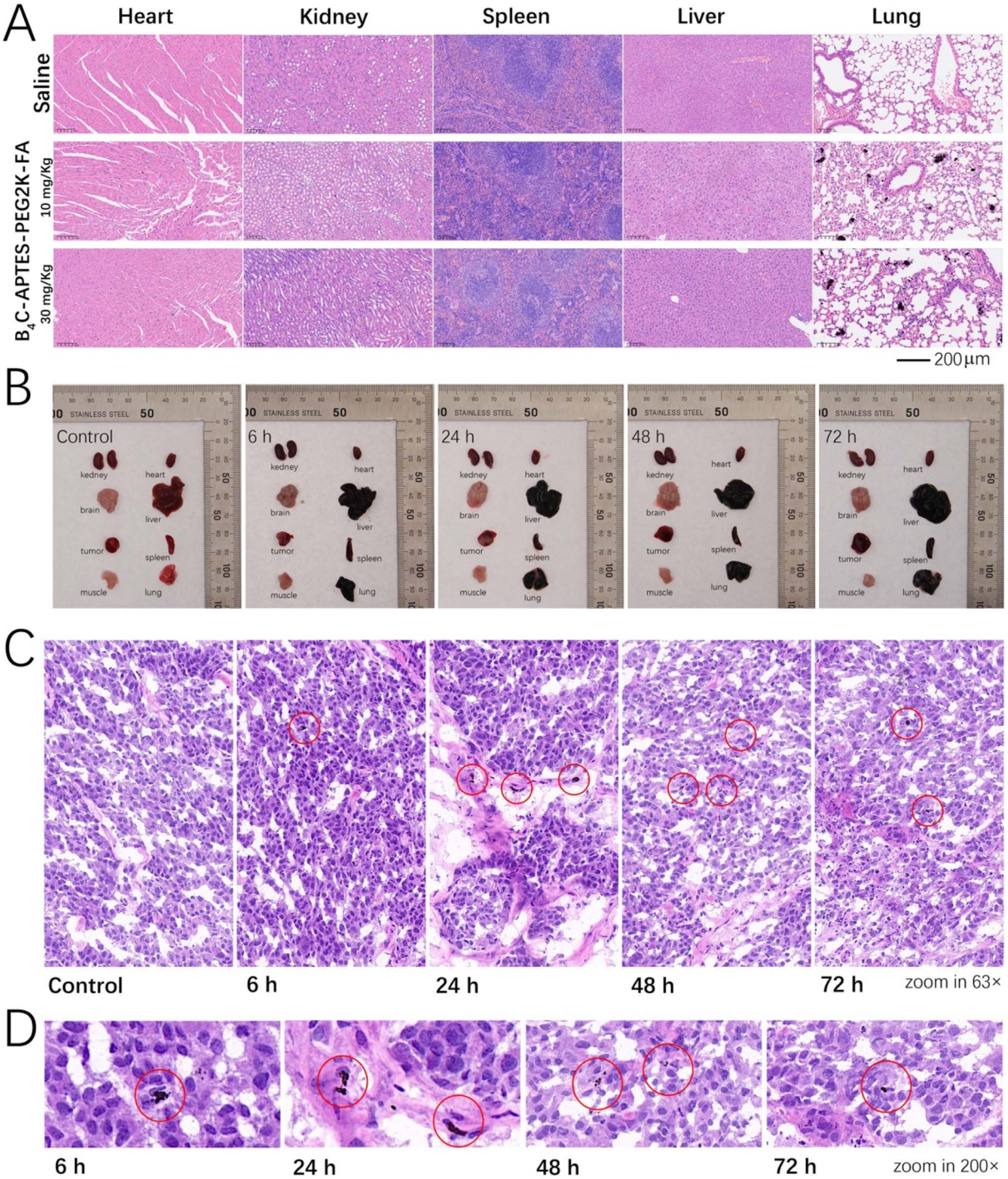

Fig. 4 *In vivo* safety assay results and biodistribution of B_4C nanoparticles in mice. (A) H&E-stained paraffin sections of the vital organs. (B) Typical images of anatomical organs of NCG mouse. (C) H&E-stained frozen sections of the tumor (63× magnification). (D) H&E-stained frozen sections of the tumor (200× magnification).

presence of a limited number of black particles within the slice. At 24 hours post-injection, these black particles had become more widely distributed within the tumor, including both small single particles and large aggregated clusters (red circles in Fig. 4C). However, at 48 and 72 hours after injection, the presence of small black particles within the tumor was observed to be stable. These observations confirm the successful penetration of the NPs into the tumor tissue due to the EPR effect of the tumor. This finding underscores the potential of these NPs to target tumor sites, a critical consideration for therapeutic applications.

To quantitatively assess the biodistribution of NPs in tumor-bearing NCG mice, a comprehensive dissection procedure was performed at four time points (6 hours, 24 hours, 48 hours, and

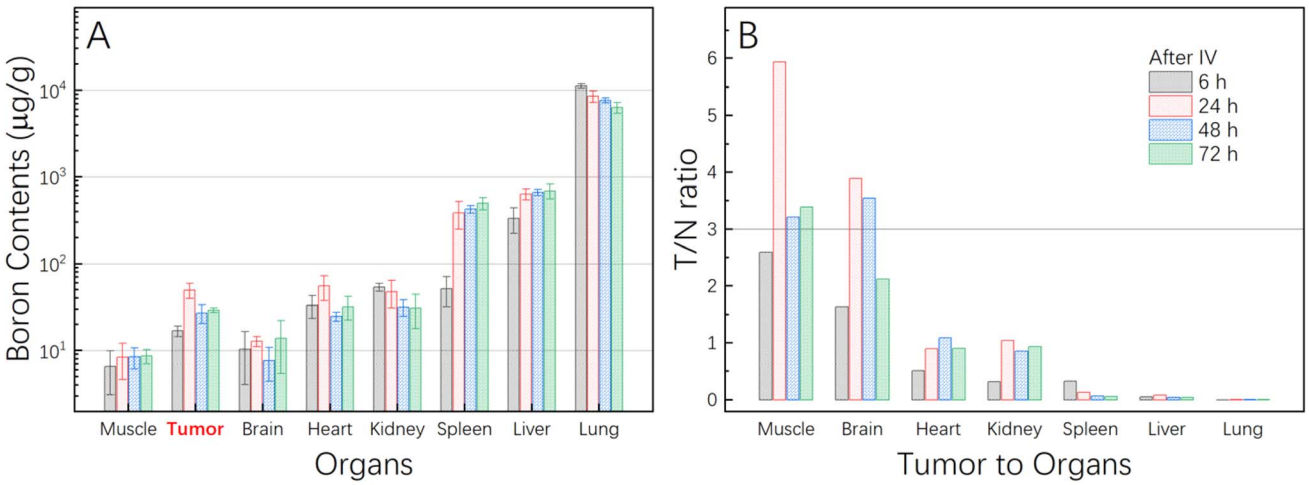

Fig. 5 Quantitative analysis of B_4C in mice. (A) Boron contents in vital organs. (B) Tumor-to-normal tissue ratio of boron contents in major tissues and organs (the nanoparticles B_4C-APTES-PEG2K-FA were injected at a dosage of 30 mg kg^{-1}).

72 hours post-injection). The dissection process included the removal of heart, liver, spleen, lung, kidney, tumor, whole brain, and muscle samples from the mice. After digestion, the boron content was measured by ICP-OES, and T/N (the ratio of boron content in the tumor to that in the normal tissue) was calculated. As illustrated in Fig. 5A, the biodistribution of boron in murine subjects revealed that the highest concentrations of the B element were observed in the lung, followed by the liver, spleen, kidney, heart, and tumor. Conversely, the brain and muscle exhibited the lowest concentration.

In the case of tumor tissue, the boron content demonstrated an initial increase, followed by a subsequent decrease, and then remained stable during the investigation period. Specifically, 6 hours after the injection, the boron concentration in the tumor was 16.90 ± 2.35 μg g^{-1}, which was calculated as pure boron atom in dried organs. This concentration peaked at 24 hours, reaching 49.66 ± 10.08 μg g^{-1}, and thereafter began to decline. At 48 hours and 72 hours post-injection, the concentrations were 27.04 ± 6.47 μg g^{-1} and 29.22 ± 1.85 μg g^{-1}, respectively. During neutron irradiation, the required amount of ^{10}B to enter each gram of tumor was estimated to be between 20 and 50 μg.[15] Consequently, the B content in the tumor was found to be sufficient to meet the treatment requirements lasting between 24- and 72-hours post-injection, with the optimal time point being approximately 24 hours. Table S3.3† presents the percentage of the drug distributed in each gram of tissue (or organ) relative to the initial injected dose (ID). From this table, we can observe that the tumor achieved 1.66% ID per g at 24 hours. This value was higher than the dose in the kidneys, which was 1.58% ID per g.

The temporal progression of boron content exhibited variability among diverse organs and tissues. Specifically, the content of boron in the lung and kidney demonstrated a downward trend, which may be attributable to the normal metabolism of nanoparticles in the lungs and kidneys of NCG mice, resulting in the excretion of boron from the body and gradual reduction in its concentration.

The BNCT approach necessitates the selective targeting of boron agents to the tumor site and tumor cells, thereby ensuring the accumulation of boron within the tumor while minimizing its accumulation in normal tissues. To ensure the efficacy of the treatment, the tumor-to-normal tissue (T/N) ratio of boron contents must exceed 3. As illustrated in Fig. 5B, in muscle tissue, the T/N ratio reached its peak at 24 hours, with a value of 5.9, and remained above 3 at both 48 and 72 hours. The large particle size of the boron agent facilitated its engulfment by numerous phagocytes in the organ, leading to limited distribution in the tumor. However, some nanoparticles were still absorbed by the tumor due to the EPR effect.

Similarly, to achieve an optimal therapeutic effect, the tumor-to-blood (T/B) ratio of boron contents should also surpass 3 (T/B > 3). Despite these efforts, attempts to collect blood samples from NCG mice for the calculation of T/B proved unsuccessful, as no significant concentrations of boron were detected in the blood. This can be attributed to the limited volume of blood, which rendered detection after digestion difficult. Additionally, the presence of large-sized NPs may have hindered their long-term circulation in the blood, as they could have been rapidly engulfed by phagocytic cells or captured by proteins prior to testing. Therefore, the T/B ratio was not reported in this study.

4. Conclusions

In summary, B_4C nanoparticles were successfully subjected to chemical modification, with the FA moiety being linked to the surface of the particles with or without PEG segments acting as linkers. It was demonstrated that FA and its derivatives could be effectively coupled onto the nanoparticles, with a maximum weight content of 10%. Over the course of 60 days of continuous observation, the FA-modified boron carbide series products demonstrated stability within the PBS solution. *In vitro* biosafety assays encompassing hemolysis and cytotoxicity experiments substantiated the nanoparticles' favorable blood

compatibility and minimal cytotoxicity at low dosages. Furthermore, cell uptake experiments revealed that tumors with high FR expression exhibited a greater capacity to adsorb the nanoparticles. The *in vivo* exploration of the modified B_4C-APTES-PEG2K-FA nanoparticles revealed no metabolic disorders or overt abnormalities in liver and kidney function, as indicated by routine blood and blood biochemistry tests. Furthermore, the biodistribution of the nanoparticles was investigated through the analysis of stained tissue sections and ICP-OES quantitative studies. It was found that the nanoparticles predominantly accumulated in the lung, liver, and spleen. The concentration of boron in the tumor initially increased, then decreased gradually, and ultimately stabilized, at approximately 50 μg per g tissue after 24 hours of tail vein injection. Additionally, the tumor-to-muscle and tumor-to-brain ratios of boron contents were found to exceed 3 following 24 hours of intravenous injection, meeting the relevant requirements for BNCT treatment. The functionalized nanoparticles in this work could serve as potential valuable boron agents for BNCT.

Data availability

The data supporting this article have been included as part of the ESI.†

Conflicts of interest

The authors declare no conflicts of interest.

Acknowledgements

The authors would like to acknowledge the financial support provided by the National Key R&D Program of China (2022YFA01203002) and Jiangsu Provincial Science and Technology Plan Special Fund (BM2023008). Additionally, the research endeavors have received partial funding from the Fundamental Research Funds for the Central Universities, as well as from the MOE Key Laboratory of High-Performance Polymer Materials & Technology at Nanjing University (Grand No. 020514380274).

References

1 H. Sung, J. Ferlay, R. L. Siegel, M. Laversanne, I. Soerjomataram, A. Jemal and F. Bray, Global cancer statistics 2020: GLOBOCAN estimates of incidence and mortality worldwide for 36 cancers in 185 countries, *CA-Cancer J. Clin.*, 2021, **71**(3), 209–249.

2 G. Locher, Biological effects and therapeutic possibilities of neutrons, *Am. J. Roentgenol. Radium Ther.*, 1936, **36**, 1–13.

3 L. E. Farr, W. H. Sweet, H. B. Locksley and J. S. Robertson, Neutron capture therapy of gliomas using boron, *Trans. Am. Neurol. Assoc.*, 1954, **13**, 110–113.

4 R. F. Barth, Z. Z. Zhang and T. Liu, A realistic appraisal of boron neutron capture therapy as a cancer treatment modality, *Cancer Commun.*, 2018, **38**, 36.

5 J. Hiratsuka, N. Kamitani, R. Tanaka, E. Yoden, R. Tokiya, M. Suzuki, R. F. Barth and K. Ono, Boron neutron capture therapy for vulvar melanoma and genital extramammary Paget's disease with curative responses, *Cancer Commun.*, 2018, **38**, 38.

6 M. Suzuki, K. Endo, H. Satoh, Y. Sakurai, H. Kumada, H. Kimura, S. Masunaga, Y. Kinashi, K. Nagata, A. Maruhashi and K. Ono, A novel concept of treatment of diffuse or multiple pleural tumors by boron neutron capture therapy (BNCT), *Radiother. Oncol.*, 2008, **88**(2), 192–195.

7 M. Suzuki, Y. Sakurai, S. Hagiwara, S. Masunaga, Y. Kinashi, K. Nagata, A. Maruhashi, M. Kudo and K. Ono, First attempt of boron neutron capture therapy (BNCT) for hepatocellular carcinoma, *Jpn. J. Clin. Oncol.*, 2007, **37**(5), 376–381.

8 W. H. Jin, C. Seldon, M. Butkus, W. Sauerwein and H. B. Giap, A Review of Boron Neutron Capture Therapy: Its History and Current Challenges, *nt. J. Part. Ther.*, 2022, **9**(1), 71–82.

9 R. F. Barth and A. H. Soloway, Boron neutron capture therapy of brain tumors - Current status and future prospects - Preface, *J. Neuro-Oncol.*, 1997, **33**(1–2), 3–7.

10 M. Suzuki, Boron neutron capture therapy (BNCT): a unique role in radiotherapy with a view to entering the accelerator-based BNCT era, *Int. J. Clin. Oncol.*, 2020, **25**(1), 43–50.

11 R. F. Barth, P. Mi and W. L. Yang, Boron delivery agents for neutron capture therapy of cancer, *Cancer Commun.*, 2018, **38**, 35.

12 T. Luo, W. Z. Huang, F. Y. Chu, T. Y. Zhu, B. Feng, S. Huang, J. Hou, L. Y. Zhu, S. H. Zhu and W. B. Zeng, The Dawn of a New Era: Tumor-Targeting Boron Agents for Neutron Capture Therapy, *Mol. Pharm.*, 2023, **20**(10), 4942–4970.

13 Y. Mishima, M. Ichihashi, S. Hatta, C. Honda, K. Yamamura, T. Nakagawa, H. Obara, J. Shirakawa, J. Hiratsuka, K. Taniyama, C. Tanaka, K. Kanda, T. Kobayashi, T. Sato, M. R. Ishida, Y. Ujeno, M. Takahashi, M. Abe and T. Nozaki, First human clinical trial of melanoma neutron capture. Diagnosis and therapy, *Strahlenther. Onkol.*, 1989, **165**(2–3), 251–254.

14 H. Hatanaka, Clinical-Results Of Boron Neutron-Capture Therapy, *International Workshop on Neutron Beam Design, Development, and Performance for Neutron Capture Therapy*, Mit, Cambridge, Ma, 1989, pp. 15–21.

15 P. Coghi, J. X. Li, N. S. Hosmane and Y. H. Zhu, Next generation of boron neutron capture therapy (BNCT) agents for cancer treatment, *Med. Res. Rev.*, 2023, **43**(5), 1809–1830.

16 A. Gubernat, W. Pichór, D. Zientara, M. M. Bucko, L. Zych and D. Kozien, Direct synthesis of fine boron carbide powders using expanded graphite, *Ceram. Int.*, 2019, **45**(17), 22104–22109.

17 D. Kozien, B. Szermer-Olearnik, A. Rapak, A. Szczygiel, N. Anger-Gora, J. Boratynski, E. Pajtasz-Piasecka, M. M. Bucko and Z. Pedzich, Boron-Rich Boron Carbide Nanoparticles as a Carrier in Boron Neutron Capture Therapy: Their Influence on Tumor and Immune Phagocytic Cells, *Materials*, 2021, **14**(11), 3010.

18 H. Türkez, M. E. Arslan, E. Sönmez, F. Geyikoglu, M. Açikyildiz and A. Tatar, Microarray assisted toxicological investigations of boron carbide nanoparticles on human primary alveolar epithelial cells, *Chem.-Biol. Interact.*, 2019, **300**, 131–137.

19 M. W. Mortensen, P. G. Sorensen, O. Björkdahl, M. R. Jensen, H. J. G. Gundersen and T. Bjornholm, Preparation and characterization of Boron carbide nanoparticles for use as a novel agent in T cell-guided boron neutron capture therapy, *Appl. Radiat. Isot.*, 2006, **64**(3), 315–324.

20 P. Singh, M. Kaur, K. Singh, R. Meena, M. Kumar, J.-H. Yun, A. Thakur, F. Nakagawa, M. Suzuki, H. Nakamura and A. Kumar, Fluorescent boron carbide quantum dots synthesized with a low-temperature solvothermal approach for boron neutron capture therapy, *Phys. E*, 2021, **132**, 114766.

21 Y. Q. Wang, G. Reina, H. G. Kang, X. X. Chen, Y. J. Zou, Y. Ishikawa, M. Suzuki and N. Komatsu, Polyglycerol Functionalized ^{10}B Enriched Boron Carbide Nanoparticle as an Effective Bimodal Anticancer Nanosensitizer for Boron Neutron Capture and Photothermal Therapies, *Small*, 2022, **18**(37), 2204044.

22 Y. G. Assaraf, C. P. Leamon and J. A. Reddy, The folate receptor as a rational therapeutic target for personalized cancer treatment, *Drug Resistance Updates*, 2014, **17**(4–6), 89–95.

23 D. Chuan, M. Mu, H. Hou, N. Zhao, J. L. Li, A. P. Tong, B. W. Zou, H. F. Chen, B. Han and G. Guo, Folic acid-functionalized tea polyphenol as a tumor-targeting nano-drug delivery system, *Mater. Des.*, 2021, **206**, 109805.

24 A. Narmani, M. Rezvani, B. Farhood, P. Darkhor, J. Mohammadnejad, B. Amini, S. Refahi and N. A. Goushbolagh, Folic acid functionalized nanoparticles as pharmaceutical carriers in drug delivery systems, *Drug Dev. Res.*, 2019, **80**(4), 404–424.

25 H. Maeda, The 35th Anniversary of the Discovery of EPR Effect: A New Wave of Nanomedicines for Tumor-Targeted Drug Delivery-Personal Remarks and Future Prospects, *J. Pers. Med.*, 2021, **11**(3), 229.

26 C. Achilli, S. Grandi, A. Ciana, G. F. Guidetti, A. Malara, V. Abbonante, L. Cansolino, C. Tomasi, A. Balduini, M. Fagnoni, D. Merli, P. Mustarelli, I. Canobbio, C. Balduini and G. Minetti, Biocompatibility of functionalized boron phosphate (BPO_4) nanoparticles for boron neutron capture therapy (BNCT) application, *Nanomed. Nanotechnol. Biol. Med.*, 2014, **10**(3), 589–597.

27 S. Grandi, A. Spinella, C. Tomasi, G. Bruni, M. Fagnoni, D. Merli, P. Mustarelli, G. F. Guidetti, C. Achilli and C. Balduini, Synthesis and characterisation of functionalized borosilicate nanoparticles for boron neutron capture therapy applications, *J. Sol-Gel Sci. Technol.*, 2012, **64**(2), 358–366.

28 O. Postel and J. Heberlein, Deposition of boron carbide thin film by supersonic plasma jet CVD with secondary discharge, *Surf. Coat. Technol.*, 1998, **108–109**, 247–252.

29 L. G. Jacobsohn, R. K. Schulze, M. da Costa and M. Nastasi, X-ray photoelectron spectroscopy investigation of boron carbide films deposited by sputtering, *Surf. Sci.*, 2004, **572**(2–3), 418–424.

30 R. Q. Bao and D. B. Chrisey, Chemical states of carbon in amorphous boron carbide thin films deposited by radio frequency magnetron sputtering, *Thin Solid Films*, 2010, **519**(1), 164–168.

31 N. Singh, S. K. Sahoo and R. Kumar, Hemolysis tendency of anticancer nanoparticles changes with type of blood group antigen: An insight into blood nanoparticle interactions, *Mater. Sci. Eng. C*, 2020, **109**, 110645.

32 D. J. Schaer, F. Vinchi, G. Ingoglia, E. Tolosano and P. W. Buehler, Haptoglobin, hemopexin, and related defense pathways—basic science, clinical perspectives, and drug development, *Front. Physiol.*, 2014, **5**, 415.

33 S. B. Rao and C. P. Sharma, Use of chitosan as a biomaterial: Studies on its safety and hemostatic potential, *J. Biomed. Mater. Res.*, 1997, **34**(1), 21–28.

34 J. Zhang, X. G. Chen, Y. Y. Li and C. S. Liu, Self-assembled nanoparticles based on hydrophobically modified chitosan as carriers for doxorubicin, *Nanomed. Nanotechnol. Biol. Med.*, 2007, **3**(4), 258–265.

35 H. Liu, Z. Li, Y. Sun, X. Geng, Y. Hu, H. Meng, J. Ge and L. Qu, Synthesis of Luminescent Carbon Dots with Ultrahigh Quantum Yield and Inherent Folate Receptor-Positive Cancer Cell Targetability, *Sci. Rep.*, 2018, **8**(1), 1086.

36 L. B. Tian, H. Z. Guo, Y. F. Bai, Y. T. Zhong, S. F. Zhou and L. C. Chen, One-pot preparation of biocompatible folate-functionalized graphitic carbon nitride quantum dots for targeted bioimaging, *Chem. Eng. J.*, 2022, **446**, 136932.

37 G. M. Saladino, P. H. Chao, B. Brodin, S. D. Li and H. M. Hertz, Liposome biodistribution mapping with *in vivo* X-ray fluorescence imaging, *Nanoscale*, 2024, **16**(37), 17404–17411.

38 T. L. Botha, E. E. Elemike, S. Horn, D. C. Onwudiwe, J. P. Giesy and V. Wepener, Cytotoxicity of Ag, Au and Ag-Au bimetallic nanoparticles prepared using golden rod (Solidago canadensis) plant extract, *Sci. Rep.*, 2019, **9**(1), 4169.

39 D. Lei, W. Yang, Y. Q. Gong, J. Jing, H. L. Nie, B. Yu and X. L. Zhang, Non-covalent decoration of carbon dots with folic acid via a polymer-assisted strategy for fast and targeted cancer cell fluorescence imaging, *Sens. Actuators, B*, 2016, **230**, 714–720.

40 J. L. Zhang, X. W. Zhao, M. Xian, C. Dong and S. M. Shuang, Folic acid-conjugated green luminescent carbon dots as a nanoprobe for identifying folate receptor-positive cancer cells, *Talanta*, 2018, **183**, 39–47.

41 R. J. Wu, C. S. Liang, J. C. Zou, C. Li, Y. Q. Yan, X. Hu and X. M. Ling, Detection of membrane receptors on per tumor cell by nonimmobilized cell capillary electrophoresis and a mathematic model, *Talanta*, 2021, **222**, 121425.

42 Q. Huang, Y. Yang, T. Zhao, Q. Chen, M. Liu, S. Ji, Y. Zhu, Y. Yang, J. Zhang, H. Zhao, Y. Nan and K. Ai, Passively-targeted mitochondrial tungsten-based nanodots for

efficient acute kidney injury treatment, *Bioact. Mater.*, 2023, **21**, 381–393.

43 E. Blanco, H. Shen and M. Ferrari, Principles of nanoparticle design for overcoming biological barriers to drug delivery, *Nat. Biotechnol.*, 2015, **33**(9), 941–951.

44 H. Maeda, Tumor-Selective Delivery of Macromolecular Drugs via the EPR Effect: Background and Future Prospects, *Bioconjugate Chem.*, 2010, **21**(5), 797–802.

45 M. Longmire, P. L. Choyke and H. Kobayashi, Clearance properties of nano-sized particles and molecules as imaging agents: considerations and caveats, *Nanomedicine*, 2008, **3**(5), 703–717.